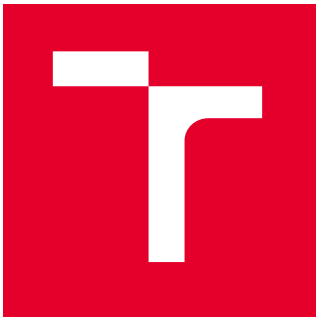

BRNO UNIVERSITY OF TECHNOLOGY

VYSOKÉ UČENÍ TECHNICKÉ V BRNĚ

FACULTY OF MECHANICAL ENGINEERING

FAKULTA STROJNÍHO INŽENÝRSTVÍ

INSTITUTE OF MATHEMATICS

ÚSTAV MATEMATIKY

HIGH PRECISION SUB-PIXEL IMAGE REGISTRATION METHODS AND THEIR APPLICATIONS IN ASTROPHYSICS

HIGH PRECISION SUB-PIXEL IMAGE REGISTRATION METHODS AND THEIR APPLICATIONS IN ASTROPHYSICS

DOCTORAL THESIS - SHORT VERSION

DIZERTAČNÍ PRÁCE - ZKRÁCENÁ VERZE

AUTHOR — Ing. Zdeněk Hrazdíra

AUTOR PRÁCE

SUPERVISOR — prof. RNDr. Miloslav Druckmüller, CSc.

ŠKOLITEL

BRNO 2022

Abstract
Many scientific observations and measurement techniques, that rely on data from images, include an image registration step. The results of such techniques thus often heavily rely on the precision of the image registration. This thesis describes a novel, robust and highly accurate sub-pixel image registration method (based on the standard phase correlation image registration method), and its applications in various fields.

Abstrakt
Mnoho vědeckých pozorování a měření, které pracují s obrazovými daty, obsahují krok, ve kterém je nutno dané obrazy registrovat (navzájem sesadit). Výsledky těchto metod tak často silně závisí na přesnosti registrace obrazů. Tato práce popisuje novou, robustní a vysoce přesnou metodu sub-pixelové registrace obrazů (založenou na registraci standardní fázovou korelací) a její aplikace v různých oborech.

Keywords
image registration, cross-correlation, phase correlation, Fourier transform, sub-pixel accuracy, optimization

Klíčová slova
registrace obrazů, křížová korelace, fázová korelace, Fourierova transformance, sub-pixelová přesnost, optimalizace

Contents

Introduction

The need to effectively and reliably solve the image registration problem arises in many domains, ranging from medical and satellite imaging [Jenkinson and Smith, 2001, Mahmood and Lee, 2019] to optical flow [Lefébure and Cohen, 2001], experimental mechanics [Bing et al., 2006], 3D reconstruction [Gravel et al., 2012], astrophysics [Chen et al., 2014, Zhou and Yu, 2018, Shapiro et al., 2013] and many more.

Intensity-based methods (methods based on a notion of correlation) are one of the most frequently used and widely-known techniques in this domain [Leng et al., 2019], mostly because of their relative computational efficiency, which is often achieved by a clever use of the convolution/correlation theorem together with the Fast Fourier Transform algorithm [Brigham and Morrow, 1967]. Popular intensity-based image registration methods include the cross-correlation method and the phase correlation method, upon which many of the state of the art methods are built [Debella-Gilo and Kääb, 2011, Heid and Kääb, 2012, Abdou, 1998, Foroosh et al., 2002, Balci and Foroosh, 2006].

Contrary to intensity-based image registratiom methods, feature-based methods do not produce a single image shift estimate for the whole registered image pair, but a set of varying image shift estimates at multiple automatically detected locations. Feature-based image registration methods are therefore well suited for registering images with non-uniform motion. Many feature detection and description methods exist, each with its own advantages and drawbacks, which include speed, accuracy, robustness, ease of use (number of parameters) and availability (license type). Popular and frequently used feature detectors/descriptors include ORB [Rublee et al., 2011], SIFT [Lowe, 1999] and SURF [Bay et al., 2008].

The main results of this work include various novel astrophysical applications of state of the art intensity-based and feature-based image registration methods, along with a detailed description and evaluation of a novel, robust and highly accurate sub-pixel image registration method and some of its many potential applications. The novel Iterative Phase Correlation (IPC) method is an extension of the standard phase correlation method of image registration to the sub-pixel domain. The high sub-pixel accuracy of the IPC method is mainly suited for scientific measurements using high quality image data.

A general overview of the most frequently used image registration techniques can be found in Chapter 1, containing popular intensity-based methods in Section 1.1 and popular feature-based methods in Section 1.2. The novel IPC image registration method is described in detail in Chapter 2. Rigorous sub-pixel accuracy measurements for various image sizes and noise levels and comparison with other image registration methods can be found in Section 2.7. Various novel astrophysical applications of the IPC algorithm and other image registration algorithms are presented in Chapter 3, including dissimilar image alignment (3.1), solar differential rotation speed measurement (3.2) and solar wind speed measurement (3.3).

Chapter 1

Image registration methods

1.1 Intensity-based methods

The cross-correlation function describes a measure of similarity between two input signals, based on their relative displacement. Thus, for each pair of sufficiently similar regions in the two correlated signals, the cross-correlation function will contain a local maximum - a distinct "peak" at the location of the corresponding relative displacement. The value of the cross-correlation function in each of these local maxima depends on the extent of similarity, and therefore may vary significantly across all local maxima.

To measure the relative x and y shift (denoted Δx and Δy) between images $I_1(x, y)$ and $I_2(x, y)$ via the cross-correlation image registration method, firstly, the Fourier transform of the first image (denoted $\mathcal{F}\{I_1(x, y)\}$) and the complex conjugate of the Fourier transform of the second image (denoted $\overline{\mathcal{F}\{I_2(x, y)\}}$) are computed. These Fourier spectra are then multiplied element-wise (denoted by $\odot$), and an inverse Fourier transform of the result is calculated. This results in the discrete cross-correlation landscape $C(x, y)$.

To produce the estimate of the image shift $[\Delta x, \Delta y]$, the location of the maximum correlation value (maximum element in $C(x, y)$) is found. The $[x, y]$ coordinates of the maximum correlation location are then the corresponding cross-correlation image registration shift estimates, mathematically expressed as

$$[\Delta x, \Delta y] = \arg\max_{x,y} \left(\mathcal{F}^{-1} \left\{ \mathcal{F}\{I_1(x, y)\} \odot \overline{\mathcal{F}\{I_2(x, y)\}} \right\} \right). \tag{1.1}$$

Similarly to the cross-correlation function, the phase correlation function also describes the similarity between two input signals, based on their relative displacement. The process of obtaining the correlation landscape with phase correlation is also very similar, the only difference being that the cross power

spectrum (the result of multiplying the Fourier transforms together) is normalized before the inverse Fourier transform is applied, mathematically expressed as

$$[\Delta x, \Delta y] = \underset{x,y}{\arg\max} \left(\mathcal{F}^{-1} \left\{ \frac{\mathcal{F}\{I_1(x,y)\} \odot \overline{\mathcal{F}\{I_2(x,y)\}}}{\left| \mathcal{F}\{I_1(x,y)\} \odot \overline{\mathcal{F}\{I_2(x,y)\}} \right|} \right\} \right). \tag{1.2}$$

The resulting image shift estimate obtained by the standard cross-correlation and phase correlation methods is inherently restricted to integer values, since it directly corresponds to the location of maximal correlation. Multiple newer image registration techniques aim to improve the registration accuracy of the phase correlation method by extending it to the sub-pixel domain [Alba et al., 2015]. These correlation extensions employ many various ideas, e.g. image upsampling, quadratic/Gaussian/sinc fitting in correlation space, linear fitting in frequency space, local correlation center of mass (centroid), upsampling in the frequency space and more.

1.2 Feature-based methods

For some types of image registration tasks, using intensity-based (correlation) image registration algorithms yields very poor results. Such tasks mostly include registering image pairs, that contain multiple distinct regions, which are shifted by a different amount and/or in a different direction, or registering images with non-stationary regions and a stationary background. In these cases, intensity-based image registration methods have difficulty estimating the correct image shift, since there is no single correct underlying image shift for the whole image. The correlation landscapes for such image pairs often include multiple similarly strong peaks, and for this reason, the resulting image shift estimates become unreliable and tend to oscillate between multiple values. The only possible solution (using intensity-based methods) in such case is to partition the registered images into equally-sized sub-regions and estimate the image shift individually for each sub-region. However, this approach only works, if the non-uniform overall image shift becomes sufficiently close to being uniform in each sub-region. It might be challenging to estimate the correct shape and number (and therefore size) of sub-regions in the partition, so that each sub-region sufficiently fulfills the image shift uniformity condition. Furthermore, for small sub-regions, the resolution might become insufficient to obtain a reliable image shift estimate.

The feature-based image registration process consists of three main steps - feature detection, feature description and feature matching. Firstly, both images are scanned and points of interest (keypoints) are detected in each

image (feature detection). Secondly, feature descriptors are computed for each of the detected keypoints, carrying information about the local neighborhood of the keypoint (feature description). Finally, the descriptors of the keypoints detected in the first image are matched with the descriptors of the keypoints detected in the second image, yielding a set of matching keypoint pairs. The resulting image shift estimate for the given keypoint pair is then simply the difference between the corresponding keypoint locations.

Chapter 2

The Iterative phase correlation method

The Iterative Phase Correlation (IPC) image registration method is a sub-pixel extension of the standard phase correlation algorithm. The registration accuracy improvement is obtained mainly by the means of cross-power spectrum filtering, correlation interpolation and iterative sub-pixel centroid refinement, all of which will be discussed in the sections to come. It is important to mention, that exactly the same extension can also be applied to the cross-correlation algorithm. However, the standard phase correlation approach frequently outperforms the standard cross-correlation approach (in the sense of accuracy, resolution and brightness invariance), and thus is the preferred candidate for further attempts of accuracy improvement.

2.1 Image windowing

Before the first and most computationally expensive phase correlation step of computing the discrete Fourier transforms (DFTs) of both input images, it often proves beneficial to multiply both images by a window function $W(x, y)$ (or simply just window), to reduce the effects of spectral leakage. The term "spectral leakage" originates from the fact, that the DFT power of a given underlying image frequency often "leaks" to the adjacent frequency bins. The effects of spectral leakage are present in all DFTs of aperiodic images, due to the periodic input assumption of the discrete Fourier transform.

The simplest approach to mitigate such negative DFT effects is setting all pixels on the image boundary to the same value (usually zero), or letting the image pixels unmodified but increasing the image size by adding black (zero) borders on all sides, which effectively makes the image periodic in both x and y directions. This approach, however, introduces large gradients near the image

boundary for most real-world images. The resulting DFT power spectrum is then often corrupted with large values at high frequencies, which arise as a direct consequence of the large image boundary gradients. This simple constant boundary approach thus resolves one negative DFT effect, but introduces another, which often affects the resulting DFT spectrum even more severely. As previously mentioned, the approach, which then usually works the best, is the multiplication of the whole image by a window function $W(x, y)$, which modifies the image minimally near the center, and tends smoothly towards zero near the image borders. Such window then does not introduce any significant high frequency noise to the resulting DFT, while mitigating the spectral leakage effect.

2.2 Cross-power spectrum filtering

The first substantial deviation of the IPC method from the standard phase correlation algorithm is the addition of adjustable cross-power spectrum filtering. The filtering is applied to the normalized cross power spectrum $\hat{CP}(x, y)$ of the input images. The motivation behind the use of a cross-power spectrum filter is twofold. Firstly, as is usual in signal processing, higher spatial frequencies often mostly contain the information about noise, and thus should almost always be attenuated. Secondly, lower spatial frequencies mostly contain the information about the overall brightness of the image, which should not be important to the image registration algorithm. Furthermore, the overall brightness of the two input images could differ not only due to the image shift itself, but also due to some external factors, such as different image calibration or different exposure times. These external factors should not play a big role in the resulting image shift estimate, and thus the lower spatial frequencies should also be attenuated. The ideal cross-power spectrum filter for the IPC algorithm is then a band-pass filter $B(x, y)$ with adjustable parameters affecting the amount of attenuation of both lower and higher spatial frequencies. The band-pass filter can be implemented with sharp (rectangular) or smooth (Gaussian) transitions.

2.3 Correlation sub-regions and upsampling

After the inverse DFT of the band-pass filtered normalized cross power spectrum of the two windowed input images I_1 and I_2 is computed, the correlation

function

$$L^3 = \mathcal{F}^{-1}\left\{ B \odot \frac{\mathcal{F}\{I_1 \odot W\} \odot \overline{\mathcal{F}\{I_2 \odot W\}}}{\left|\mathcal{F}\{I_1 \odot W\} \odot \overline{\mathcal{F}\{I_2 \odot W\}}\right| + \xi} \right\}, \tag{2.1}$$

denoted as L^3, is obtained. The additional parameter ξ in the normalized cross-power spectrum denominator effectively prevents division by zero errors. Additionally, with larger values of ξ, the resulting correlation landscape becomes gradually more and more similar to the standard cross-correlation landscape.

Since upsampling the entire correlation landscape L^3 is unnecessary and computationally expensive, a sub-region of L^3, centered around the point of maximal correlation $L^3_{\max}$, is extracted (denoted as L^2). The size of this sub-region (denoted $\left|L^2\right|$) is a parameter and can be modified by the user. However, since the sub-region should be centered around a specific point, odd sub-region sizes are preferred, so that the specified point can correspond precisely to the central pixel.

The extracted correlation sub-region L^2 is upsampled with a two-dimensional interpolation method, yielding an upsampled version of L^2, denoted as L^{2U}. The type of the interpolation method and the size of L^{2U} (or equivalently, the correlation upsampling factor U) are additional adjustable parameters, which can be modified according to the characteristics of the input images. Most commonly used two-dimensional interpolation methods include the nearest neighbor interpolation, bilinear interpolation and bicubic interpolation.

Finally, another correlation sub-region centered around the maximal correlation point is extracted, this time from the already upsampled sub-region L^{2U}. The size of this sub-region is another modifiable parameter, however, specifying it as a ratio of $\left|L^{2U}\right|$ adds more clarity to the meaning of this parameter. With the L^1 size ratio denoted as L^1_r and satisfying $0 < L^1_r < 1$, the size of the final extracted L^1 sub-region becomes

$$\left|L^1\right| = \begin{cases} \max\left(\left\lfloor L^1_r \cdot \left|L^{2U}\right| \right\rfloor, 3\right), & \text{if } \left\lfloor L^1_r \cdot \left|L^{2U}\right| \right\rfloor \text{ odd} \\ \max\left(\left\lfloor L^1_r \cdot \left|L^{2U}\right| \right\rfloor + 1, 3\right), & \text{otherwise} \end{cases} \tag{2.2}$$

where the degenerate cases of too small sub-region sizes are solved simply by clamping the result from the bottom by introducing a maximum function with the value of 3, which is the lowest pixel size, that is odd and can still yield sub-pixel improvements during the iterative refinement process.

The L^1 sub-region represents the closest neighborhood of the maximum phase correlation point $L^3_{\max}$ of the original phase correlation landscape L^3, and will be the only region that will be updated in each iteration during the

iterative refinement process. The purpose of this region is to represent the phase correlation peak as closely as possible, all the while omitting all other irrelevant correlation variations from the rest of L^3. Since the horizontal cross sections of the phase correlation peak are always of a circular shape, filtering of the correlation values that do not contribute to the main correlation peak can be done by multiplying the entire L^1 region point-wise with a binary circular mask M, defined as

$$M(x,y) = \begin{cases} 1, & \text{if } \left(x - \frac{\left|L^1\right|}{2}\right)^2 + \left(y - \frac{\left|L^1\right|}{2}\right)^2 \leq \left(\frac{\left|L^1\right|}{2}\right)^2 \\ 0, & \text{otherwise.} \end{cases} \tag{2.3}$$

2.4 Iterative refinement

After the L^3, L^2, L^{2U} and L^1 regions are computed, the process of iterative sub-pixel refinement is started. The aim of this process is to accurately estimate the sub-pixel part of the image shift and thus improve the final registration accuracy. Since zero image shift corresponds to the central pixel of L^3, the pixel level accuracy image shift estimate $[\Delta x, \Delta y]$ can be computed simply by

$$[\Delta x, \Delta y] = L^3_{\max}[x,y] - L^3_{\text{mid}}[x,y], \tag{2.4}$$

where $L^3_{\max}[x,y]$ is the point of maximum phase correlation and $L^3_{\text{mid}}[x,y]$ is the central pixel of L^3. This is the standard phase correlation result, to which the final sub-pixel image shift estimate obtained by the iterative refinement will be added.

In each iterative refinement iteration (denoted with index i), firstly, the current circular upsampled sub-region $L^1(i)$ is computed as a sub-region of L^{2U}, centered around the current upsampled maximum phase correlation location $L^{2U}_{\max}(i)[x,y]$. Secondly, the sub-pixel centroid location $L^1_{\text{cen}}(i)[x,y]$ of the current circular upsampled sub-region $L^1(i)$ is calculated. Thirdly, the current upsampled maximum phase correlation location $L^{2U}_{\max}(i)[x,y]$ in the L^{2U} sub-region is calculated by adding the integer part of the current relative $L^1(i)$ centroid location (relative to the L^1 origin $L^1_{\text{mid}}[x,y]$) to its value from the previous iteration as

$$L^{2U}_{\max}(i)[x,y] = L^{2U}_{\max}(i-1)[x,y] + \left\lfloor L^1_{\text{cen}}(i)[x,y] - L^1_{\text{mid}}[x,y] \right\rfloor. \tag{2.5}$$

This iterative process is repeated until the circular upsampled sub-region centroid location is less than 0.5 pixels away from the origin in both x and y directions, or if the maximum number of iterations (denoted $N_{\max}$) is reached. The threshold distance of 0.5 pixels reflects the fact, that the L^1 sub-region

can be moved only by an integer number of (upsampled) pixels in each iteration. Therefore, if this distance is less than 0.5 pixels in both directions, the algorithm converged and the iterative refinement process is terminated.

2.5 Rotation and scale estimation

In the general IPC image alignment procedure, estimates of the rotation and scale parameters φ and s are obtained by exploiting three important Fourier transform properties, namely the Fourier transform scale property, the fact that translation in the image domain does not affect the frequency domain magnitude spectrum and the fact that rotation in the image domain corresponds to equivalent rotation in the frequency domain. The task of rotation and scale estimation can thus be transformed into translation estimation between the log-polar transformed magnitude spectra of Fourier transforms of both images.

To significantly improve the robustness of this alignment step, two additional operations are performed. Firstly, a window (see Section 2.1) is applied to both images prior to the Fourier transform magnitude spectrum computation to reduce spectral leakage effects. Secondly, since most of the frequency power of the majority of real-world images is concentrated near the origin (at lowest frequencies), a logarithm function is applied to both magnitude spectra to increase contrast for the subsequent shift estimation.

Once the rotation and scale estimates are obtained, the second input image is rotated and scaled back by the estimated amounts. Afterwards, the sub-pixel shift between the first image and the rotated and scaled second image is calculated. The second image is then shifted back by the computed amount, completing the alignment. Both affine transformations (rotation/scale and translation) can be computed with sub-pixel precision via bilinear interpolation.

2.6 Parameter optimization

The accuracy and robustness of the IPC method is affected by multiple parameters. In some of the following sections, sensible default values of all the parameters are given and explained. These default values have been tested and work well for a wide range of image types and sizes. However, if the registration estimates are to be obtained with absolute maximum sub-pixel accuracy, the IPC parameters shall be adapted (optimized) for a particular image type. Optimal IPC parameters mainly depend on the size of the image, on the image signal-to-noise ratio and on the spatial frequency characteristics of the objects

and structures contained within the image.

The central part of any optimization problem is the objective function. In this case, there are many unique ways to quantitatively express the performance of an image registration algorithm. The most natural and general measure of sub-pixel image registration performance is the sub-pixel image registration accuracy metric, defined as

$$\varepsilon = \sqrt{(\Delta\hat{x} - \Delta x)^2 + (\Delta\hat{y} - \Delta y)^2}, \tag{2.6}$$

where $[\Delta\hat{x}, \Delta\hat{y}]$ is the refined IPC shift estimate and $[\Delta x, \Delta y]$ is the true (reference) underlying sub-pixel shift between the two input images. An image pair with a given pre-determined underlying sub-pixel shift $[\Delta x, \Delta y]$ can be obtained by artificially shifting an image via bilinear interpolation.

Firstly, to evaluate shifts of varying magnitudes and directions (and thus remove measurement bias), the sub-pixel image registration accuracy is evaluated on a linearly spaced two-dimensional grid of artificial shifts $[\Delta x, \Delta y]$, ranging from -2 to 2 pixels in each direction.

Secondly, mutually independent artificial Gaussian noise is added to each input image, to simulate noise present in real image pairs. For most accurate results, the noise characteristics of the artificial noise (mainly the mean and the standard deviation) should closely match the characteristics of the real noise in the images.

Finally, to further improve robustness, the sub-pixel image registration accuracy metric can be computed on grids of artificial image pairs from multiple images. The resulting image-average and artificial image shift grid-average sub-pixel registration accuracy can then be defined as

$$\bar{\varepsilon} = \frac{1}{N_I N_x N_y} \sum_{i=1}^{N_i} \sum_{x=1}^{N_x} \sum_{y=1}^{N_y} \sqrt{(\Delta\hat{x}_{ixy} - \Delta x_{ixy})^2 + (\Delta\hat{y}_{ixy} - \Delta y_{ixy})^2}, \tag{2.7}$$

where N_I is the number of evaluated image pairs, N_x is the number of image shift grid points in the x direction and N_y is the number of image shift grid points in the y direction.

The average sub-pixel image registration accuracy objective function is generally non-convex and non-continuous. These properties significantly reduce the number of appropriate optimizers. One of the most robust and performant non-convex non-continuous derivative-free state of the art optimizers is the Differential evolution (DE) optimizer [Price, 2013, Das and Suganthan, 2010, Pant et al., 2020]. The only inputs of the DE optimizer are the objective function and the lower and upper bounds of each of the optimized parameters. The DE optimizer then initializes a random "population" of possible solutions

$W \times H$	σ	PC	PCS	IPC	IPCO
32×32	0.00	0.392±0.147	1.344±0.556	0.079±0.033	**0.029±0.019**
32×32	0.02	0.392±0.147	1.583±0.751	0.087±0.045	**0.076±0.038**
32×32	0.05	0.401±0.158	1.734±1.177	0.171±0.089	**0.112±0.058**
64×64	0.00	0.392±0.147	0.253±0.122	0.035±0.017	**0.012±0.006**
64×64	0.02	0.392±0.147	0.321±0.151	0.040±0.020	**0.022±0.011**
64×64	0.05	0.392±0.147	0.370±0.185	0.069±0.034	**0.051±0.026**
128×128	0.00	0.392±0.147	0.239±0.080	0.036±0.017	**0.009±0.005**
128×128	0.02	0.392±0.147	0.270±0.079	0.032±0.016	**0.014±0.007**
128×128	0.05	0.392±0.147	0.244±0.089	0.041±0.020	**0.034±0.017**
256×256	0.00	0.392±0.147	0.173±0.083	0.024±0.013	**0.008±0.005**
256×256	0.02	0.392±0.147	0.170±0.064	0.028±0.014	**0.010±0.005**
256×256	0.05	0.392±0.147	0.169±0.059	0.036±0.017	**0.014±0.007**

Table 2.1: Average sub-pixel image registration accuracy and its standard deviation measured on datasets of image pairs with various sizes (width W and height H) and noise levels (standard deviation σ). Measured image registration methods: standard phase correlation (PC), OpenCV implementation of a 5×5 weighted centroid sub-pixel phase correlation (PCS), Iterative Phase Correlation (IPC), Iterative Phase correlation with optimized parameters (IPCO).

within the specified parameter bounds and then produces progressively improved parameter combinations in each iteration (evolution generation), until one of the termination criteria are met. With large enough population size, the DE optimizer is very robust in finding the global objective function optimum.

2.7 Accuracy measurements and comparison

The performance of various sub-pixel image registration methods can be objectively evaluated by the average sub-pixel image registration accuracy metric on a given dataset of shifted image pairs. The sub-pixel image registration accuracy results for various methods, image sizes and noise levels can be seen in Table 2.1.

Naturally, the accuracy results of all sub-pixel methods show a clear trend of decreasing accuracy with increasing noise levels. The standard deviation of the sub-pixel accuracy also seems to increase with increasing noise levels for all sub-pixel methods. The accuracy results of the IPC method with optimized parameters show significantly improved average sub-pixel accuracy and also improved sub-pixel accuracy standard deviation.

Chapter 3

Applications

3.1 Dissimilar image alignment

In many different fields dealing with image data (e.g. astrophotography, microscopy, satellite imaging and more), it is often necessary to compose images taken with different instruments and varying wavelengths. These images can be noticeably misaligned due to differences in instrument positions, varying times of acquisition and/or different instrument optics. Misalignments typically include a combination of image translation, image rotation and scaling. To accurately align two such images, four parameters need to be precisely estimated - translational shifts Δx and Δy in the x and y directions, rotation angle φ and a scale factor s. If these four parameters are computed with good sub-pixel accuracy, the resulting composed image can have distinctly better characteristics than a composed image obtained by standard pixel-level accuracy image registration methods.

Both correlation-based and feature-based image registration methods often fail to correctly align images with low levels of similarity. A typical application, where aligning visibly very dissimilar images with high accuracy is required, is the composition of images taken by various instruments of the Atmospheric Imaging Assembly (AIA) onboard the Solar Dynamics Observatory (SDO) [Lemen et al., 2011]. A typical example of a dissimilar image pair obtained by 304Å and 171Å SDO/AIA instruments roughly at the same moment can be seen in Fig. 3.1.

Contrary to standard rotation/scale/translation image alignment methods, the IPC general image alignment method (described in Section 2.5) can adapt to the vastly different characteristics of the input images via parameter optimization (see Section 2.6). This increases the robustness of the alignment and increases the interval of image similarity, in which the method aligns images correctly.

The IPC general image alignment procedure is demonstrated on a pair of

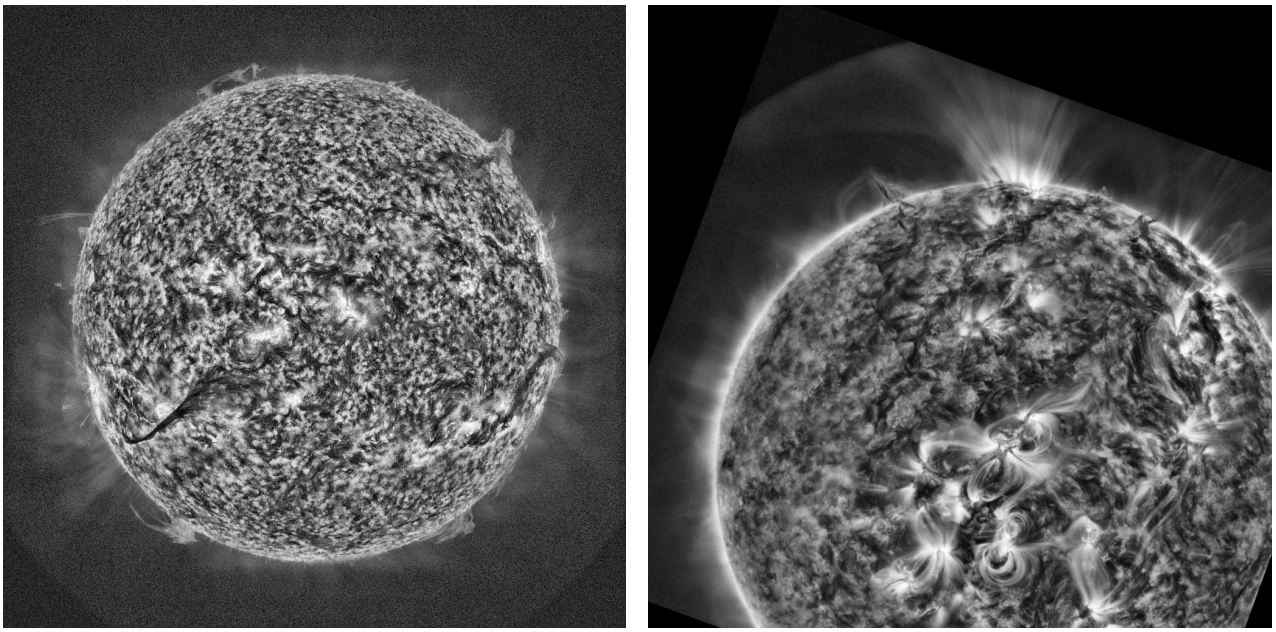

(a) (b)

Figure 3.1: An example of a significantly dissimilar image pair - contrast-enhanced 304Å (a) and 171Å (artificially transformed) (b) images taken by the Atmospheric Imaging Assembly onboard the Solar Dynamics Observatory.

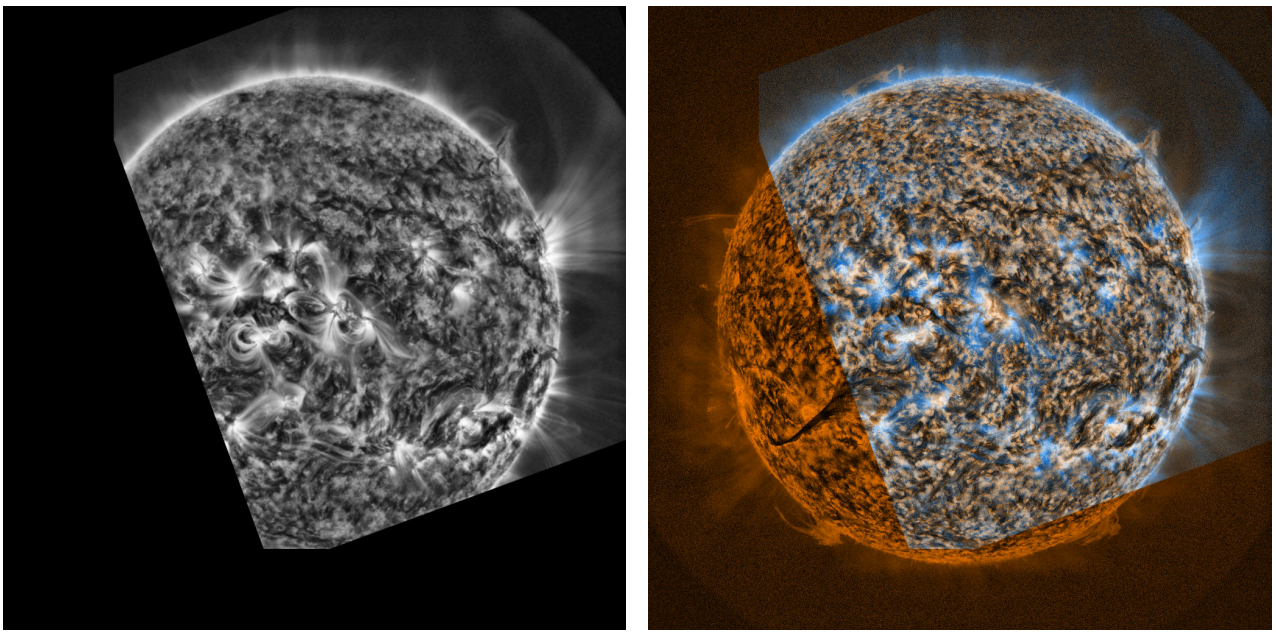

(a) (b)

Figure 3.2: General IPC image alignment of SDO/AIA 304Å and 171Å images - after rotation, scale and translation alignment. Rotation, scale and translation aligned 171Å (second) image (a), red-blue color composition of original SDO/AIA 304Å image and rotation, scale and translation aligned 171Å image (b).

dissimilar 304Å and 171Å SDO/AIA images (from Fig. 3.1). To better demonstrate the robustness of the method, the second (171Å) image is significantly artificially rotated, scaled (enlarged) and shifted prior to the alignment process. Figure 3.2 shows the second image after rotation, scale and translation (complete) alignment.

3.2 Solar differential rotation speed measurement

The identification of sunspots with features on the solar surface led to the discovery of solar rotation in the 17th century, and the variation of the rotation speed with latitude, or the differential rotation rate, by Scheiner [1630]. Advances in observational tools over the centuries led to the discovery of the oscillation modes of the Sun [Leighton et al., 1962], which established the field of helioseismology [see review by Leibacher et al., 1985]. Helioseismology further revealed that the differential rotation rate changes with depth in the convection zone [Thompson et al., 1996]. Given that the differential rotation rate is now established as a necessary mechanism for generating solar magnetic fields, i.e. the solar dynamo [Elsasser, 1950, Babcock and Babcock, 1955, Parker, 1955], the accurate determination of the differential rotation rate, starting from the solar surface, becomes even more compelling.

3.2.1 Measurement technique

The inference of the solar rotational speed at different latitudes is achieved by measuring the local west-east and north-south image shifts Δx, Δy between pairs of *Solar Dynamics Observatory* (SDO) *Helioseismic and Magnetic Imager* (HMI) continuum full disk 4096x4096 images by means of image registration. Measured image shifts are then projected onto the solar surface, allowing the corresponding angular shifts to be found.

The accuracy and reliability of the image registration technique depends heavily on the chosen time step Δt. A time step of 45s is used for all the measurements. Since the SDO/HMI images mostly contain information about the granulation on the solar surface, the time difference between the two pictures is limited by the lifetime of these granules. A typical granule has a lifetime of around 10-15 minutes, which limits the time step to around 4 minutes, to still keep good overlap and correlation between the images. The lowest possible time step of 45s is thus chosen to maximize the signal-to-noise ratio.

The local image shifts were calculated for a chosen set of pixel coordinates (and their neighborhoods) by the iterative phase correlation (IPC) sub-pixel

Flow speed curve type	A	B	C
W-E (B) (1 m.)	14.21	-1.61	-2.89
W-E (B) (1 d.)	14.27	-1.46	-2.66
W-E (N) (1 m.)	14.20	-1.93	-2.75
W-E (N) (1 d.)	14.26	-1.24	-3.47
W-E (S) (1 m.)	14.23	-1.28	-3.02
W-E (S) (1 d.)	14.28	-1.68	-1.84
N-S (N) (1 m.)	0.01	-0.82	8.18
N-S (N) (1 d.)	-0.01	-0.62	7.40
N-S (S) (1 m.)	-0.14	0.61	-5.84
N-S (S) (1 d.)	-0.27	1.29	-7.57

Table 3.1: Best (least squares) fitting coefficients A, B, C for different types of west-east (W-E) and north-south (N-S) trigonometric flow speed profile fits for northern (N), southern (S) or both (B) hemispheres, obtained from both one month (1 m.) and one day (1 d.) data sets in degrees per day according to $\omega^{\dagger}(\theta) = A + B\sin^2(\theta) + C\sin^4(\theta)$.

image registration algorithm. As the vast majority of west-east shifts between pairs of consecutive ($\Delta t = 45s$) images lie in the interval $[0.1, 0.2]$ px, the high sub-pixel precision of the IPC algorithm justifies the choice of the method. The main relevant advantage of the IPC algorithm is the potential for very high sub-pixel spatial accuracy, due to its iterative nature.

3.2.2 Measurement results

Since M sub-regions were equidistantly distributed among different latitudes on the central meridian of every picture and measurements for P picture pairs were made, very detailed 2D west-east and north-south central meridian flow speed maps with $P \times M$ resolution could be constructed for each data set. These maps can be seen in Fig. 3.3. Although the measured angular velocity clearly varies with time in a given latitude band, the temporally coherent angular velocity values in the flow speed maps demonstrate the good image registration quality. Measured from horizontally (temporally) adjacent image shifts, although being computed from entirely different pairs of images, they are very similar at each latitude, which is demonstrated by the existence of the clearly distinguishable coherent faster than average and slower than average flows in Fig. 3.3 (a).

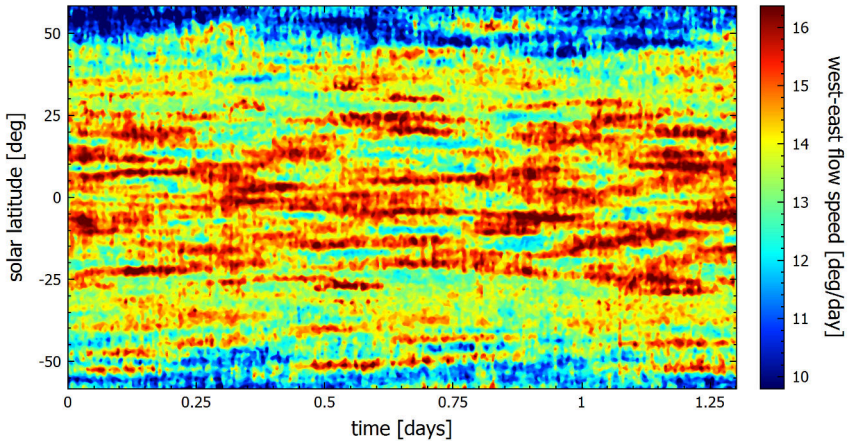

(a)

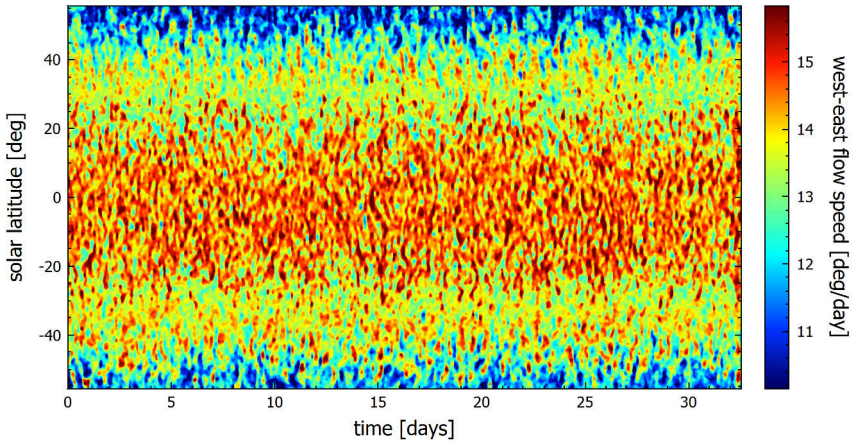

(b)

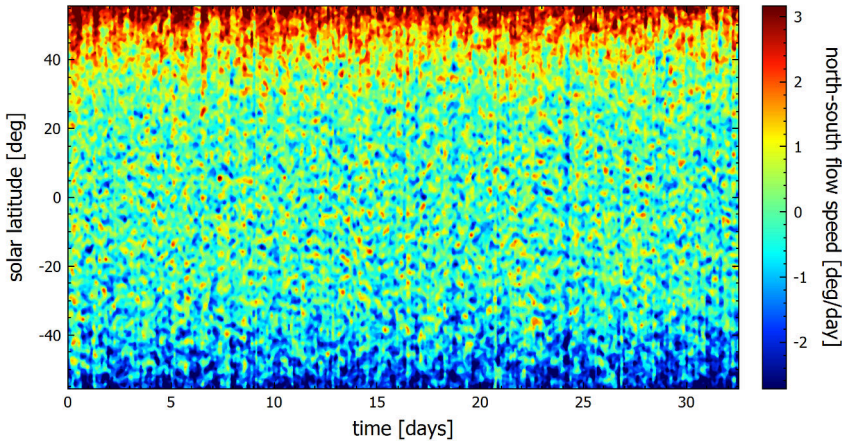

(c)

Figure 3.3: Solar west-east and north-south flow speed maps obtained from orthographically backprojecting image shifts measured on 2000 SDO/HMI continuum full-disk image pairs back onto the solar surface. First row: west-east flow speed map (a) obtained from images spanning approximately a one day period. Second row: same as the first row for a one month period. Third row: same as the first row for north-south flow.

3.3 Solar wind speed measurement

The measurement of solar wind speed from processed contrast-enhanced composite solar eclipse images [Druckmüller et al., 2006, Druckmüller, 2009] is a good example of an image registration task with non-uniform motion. The composite solar eclipse images contain both relatively stationary regions (e.g. coronal loops) and regions moving in different directions with different speeds (e.g. solar wind, solar flares, the Moon). This means, that (global) intensity-based (correlation) methods are not well suited for this task, and (local) feature-based methods need to be used instead. Furthermore, due to the contrast-enhancing process, the images often contain regions with very low average signal-to-noise ratio. The feature detector/descriptor pair thus needs to be very robust and resilient to noise.

The SURF feature detector/descriptor [Bay et al., 2008] is a very good fit for this difficult task. Furthermore, a special version of the SURF algorithm, called "upright" SURF (or U-SURF), which is not invariant to image rotation, can be used in this case, since the contrast-enhanced composite solar eclipse images do not contain any significantly scaled or rotated regions. This improves the algorithm computational performance, but more importantly in this case, also further increases the overall robustness of the results.

To detect the SURF points of interest (keypoints) in all of the contrast-enhanced solar eclipse images, a threshold Hessian determinant value of 100 was chosen. This value proved to be a good compromise between detecting many low quality features and detecting too few features. To describe the neighborhood of the detected keypoints, the U-SURF (not rotationally invariant) version of the SURF descriptor was used. Detected keypoints were matched by a brute-force L^2 similarity metric comparison of the U-SURF descriptors. The resulting matches were then filtered by Lowe's ratio test [Lowe, 2004] with a strict threshold ratio of 0.4. Overlapping matches (matches, whose initial keypoints were less than 40 pixels apart) were filtered out to improve overall clarity, always in favor of the match corresponding to a higher solar wind speed.

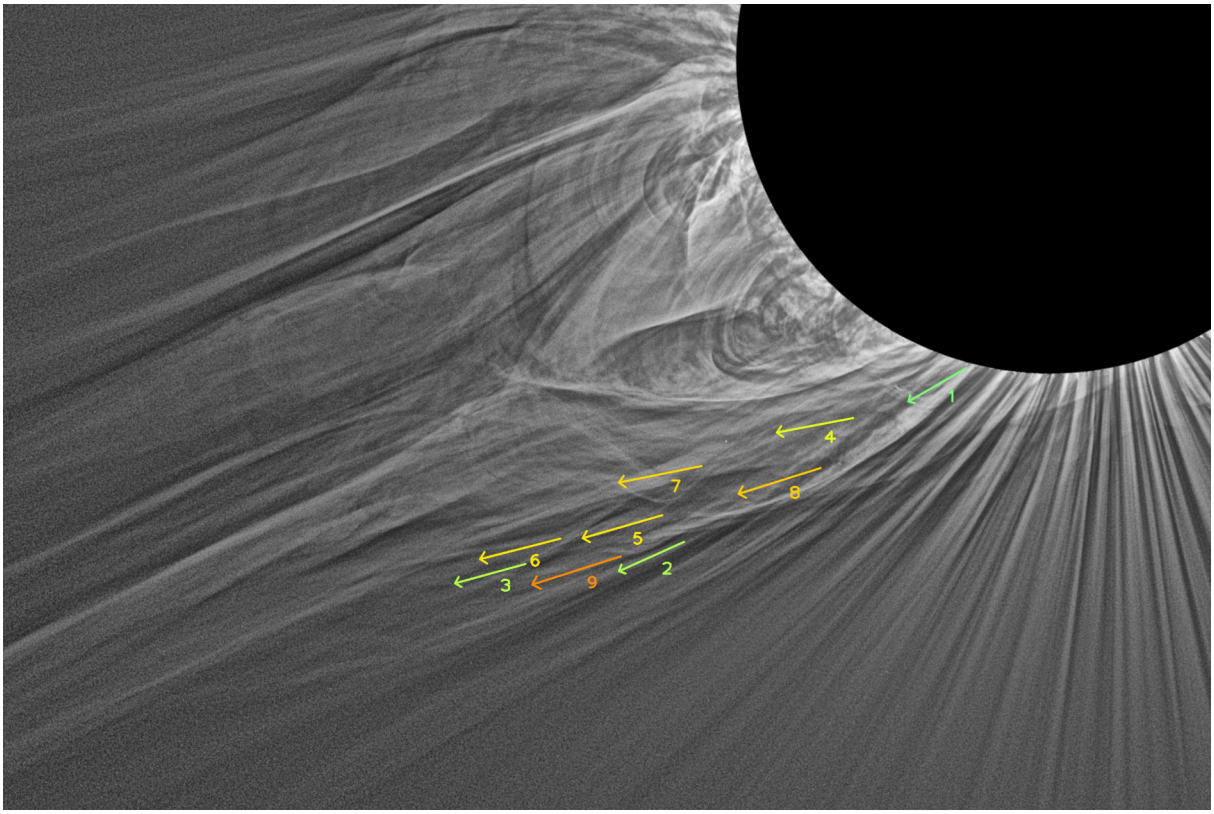

Figure 3.4: Solar wind speeds measured by the U-SURF method on sets of 10 processed composite solar eclipse images. The depicted arrows originate from the corresponding automatically detected U-SURF keypoints and are scaled and color-coded according to the relative measured solar wind speed - from blue (relatively slow) to red (relatively fast). The actual corresponding solar wind speeds (in km/s) can be calculated from the feature shifts (in pixels), the time difference between images and pixel size. Captured during the 2017 total solar eclipse at Mitchell, Oregon observing site.

Chapter 4

Summary and conclusions

The first main goal of this thesis was to develop a novel state of the art high precision image registration method focusing on sub-pixel registration accuracy. The new Iterative Phase Correlation (IPC) method is based on a reliable pixel-level accuracy phase correlation method. The IPC method is a major non-trivial extension of the standard phase correlation method, including procedures like image windowing, adjustable cross-power spectrum filtering, correlation upsampling, weighted correlation centroid computation and subsequent iterative centroid refinement. Many other sub-pixel cross-correlation and phase correlation extensions were previously developed, usually exploiting a particular idea to achieve a sub-pixel accuracy on the order of 0.1px. These ideas include image upsampling [Debella-Gilo and Kääb, 2011], fitting the correlation peak with an analytical function [Heid and Kääb, 2012, Abdou, 1998, Foroosh et al., 2002], calculating the centroid of the correlation peak [Michel and Rignot, 1999], counting the fractional number of cross-power spectrum phase cycles [Balci and Foroosh, 2006] and cross-power spectrum upsampling [Alba et al., 2015, Young and Driggers, 2006, Zhang et al., 2011]. The IPC method combines multiple of these ideas among with iterative accuracy refinement into a single reliable and efficient method regularly achieving sub-pixel accuracy on the order of 0.01px. The iterative centroid refinement step, which is the main source of high sub-pixel precision of the IPC method, is a very intuitive process, since it iteratively moves in the direction of higher average correlation.

Furthermore, all the parameters of the IPC method can be easily optimized to maximize sub-pixel accuracy for a given image dataset. The main IPC parameters affecting image windowing, cross-power spectrum filtering, correlation upsampling and iterative centroid refinement gradually adapt to a specific kind of image during a differential evolution optimization process, optimizing a sophisticated non-convex non-continuous average sub-pixel accuracy metric. The IPC optimization process does not only improve overall

average sub-pixel error (registration accuracy), but also overall sub-pixel error standard deviation (registration robustness).

Additionally, since the IPC method is an intensity-based method, it is computationally very efficient, mainly due to the use of the Fast Fourier Transform algorithm to compute the phase correlation. During each iteration in the iterative refinement process, only the centroid of a small correlation neighborhood needs to be recomputed, and thus the iterative character of the method does not significantly affect the overall computational efficiency when compared to the standard non-iterative cross-correlation and phase correlation methods. The IPC method can thus also serve as a good replacement of standard correlation methods in resource-constrained applications.

The second main goal of this work was to find novel applications of state of the art high precision image registration methods (including the newly developed IPC method), mainly focused on astrophysical measurements and observations.

The first application of high precision image registration methods researched and described in this work is the alignment of images with low levels of similarity. A good example of such image pairs are the SDO/AIA 94Å, 131Å, 171Å, 211Å, 304Å and 335Å images. Even though these images contain information about vastly different phenomena (e.g. flaring/active regions, chromosphere, corona), the IPC general image alignment method is able to align them reliably. This includes the correct estimation and correction of a combination of image scale, image rotation and image translation.

Another major astrophysical application of the IPC algorithm is the novel iterative phase correlation technique of solar differential rotation estimation. This technique offers a new method for the empirical determination of the differential rotation rate of the solar photosphere. It is based on the measurement of locally varying image shifts between consecutive ($\Delta t = 45$s) solar images. The technique was applied to SDO/HMI data and roughly covered one Carrington rotation of continuous observations from 1.1.2020 to 2.2.2020. The technique has a number of exceptional properties which make it superior to other correlation-based techniques, mainly in the domain of high spatial and temporal resolution.

The local shift measurement between two images is not limited to contrasty features like sunspots, as it can be applied even to very low contrast structures, such as granulation and/or faculae. Hence, the differential rotation rate thus determined is independent of any a priori selection of solar features, and can be successfully applied to any location in the photosphere. Unlike magnetic feature tracking methods, the IPC differential rotation measurement method does not introduce systematic measurement biases arising from the fact that the rotational velocities of various types of magnetic features do not necessarily

correspond to the underlying rotation rate of the photosphere and further depend significantly on feature size, morphology and age [Ward, 1966, Gilman and Howard, 1984, Zappala and Zuccarello, 1991].

The unprecedented $\Delta t = 45$s time step resulted in the most precise and reliable sub-pixel image shift measurements, as larger time steps correspond to significant non-uniform granulation changes, for which a sub-pixel image shift can not be measured reliably. The extreme temporal resolution of the IPC method of differential rotation measurement enables the study of short-period photospheric phenomena and the comparison of measurements on different days separated by an event that may have a global impact on the solar magnetic field, such as a solar flare or a coronal mass ejection.

Furthermore, given that the technique does not rely on visible features, it can be used throughout a full solar cycle independently of the presence of specific features in the photosphere. While methods based on solar markers yield a limited number of data points, the iterative phase correlation technique is applicable to every pixel close to central meridian within a given latitude band. This yields a unique opportunity to study the rotation rate of the Sun locally.

The method is also able to estimate the locally varying north-south shifts between consecutive solar images. Although being very small and hard to measure, the north-south image shifts obtained by the novel image registration method show coherent results, displaying a consistent global trend. The reliability of the north-south image shift measurement allows further studies of the general (not only rotational) photospheric movements with great detail. The north-south flow speed results show an overall flow towards the solar equator, with speeds becoming more significant closer to the geographic poles. Both the west-east and north-south flow speed profiles were fitted with polynomial and trigonometric curves, whose best (least squares) parameters were calculated and compared with other methods.

The reliability of the approach is underscored by the fact that the average sidereal differential rotation curve obtained is in the middle of other published results. At the same time it also clearly shows the now well established N-S rotational speed asymmetry. Furthermore, the quality of the results is further supported by the smoothness of the average west-east image shift profile obtained from a single Carrington rotation of SDO/HMI image data and also by the coherence of the measured flow speed values inferred from temporally adjacent images. As an added bonus, the novel technique described in this work allows the study of short-lived and previously undetected phenomena associated with the solar magnetic field.

Intensity-based image registration methods are not suited for all astrophysical applications. In some measurements, temporally adjacent images contain

multiple regions moving in significantly different directions and speeds. For such applications, feature-based image registration methods are more appropriate. One such astrophysical application of feature-based image registration methods described in this work is the measurement of the solar wind speed from composite solar eclipse images. In this approach, the solar wind speed is estimated from regional shifts obtained by the SURF feature detector and descriptor on multiple pairs of processed contrast-enhanced composite solar eclipse images. The region locations correspond to the automatically detected feature keypoints. To improve the robustness of this technique, only features with very high Hessian threshold are considered. Furthermore, feature pairs not passing Lowe's ratio test with a strict L^2 similarity ratio of 0.4 are discarded. The technique of feature-based image registration of pairs of contrast-enhanced composite solar eclipse images offers a novel way of solar wind speed measurement at various distances from the solar surface.

In conclusion, the high sub-pixel accuracy of the newly developed IPC image registration method is not only able to significantly improve the accuracy of some existing astrophysical measurements based on image registration techniques, but also allow novel measurements and observations in domains where image registration (or any other) techniques were previously not applicable.

Bibliography

I. E. Abdou. Practical approach to the registration of multiple frames of video images. In *Visual Communications and Image Processing'99*, volume 3653, pages 371–382. SPIE, 1998.

A. Alba, J. F. Vigueras-Gomez, E. R. Arce-Santana, and R. M. Aguilar-Ponce. Phase correlation with sub-pixel accuracy: A comparative study in 1d and 2d. *Computer Vision and Image Understanding*, 137:76–87, 2015.

H. W. Babcock and H. D. Babcock. The sun's magnetic field, 1952-1954. *The Astrophysical Journal*, 121:349, 1955.

M. Balci and H. Foroosh. Subpixel registration directly from the phase difference. *EURASIP Journal on Advances in Signal Processing*, 2006:1–11, 2006.

H. Bay, A. Ess, T. Tuytelaars, and L. Van Gool. Speeded-up robust features (surf). *Computer vision and image understanding*, 110(3):346–359, 2008.

P. Bing, X. Hui-Min, X. Bo-Qin, and D. Fu-Long. Performance of sub-pixel registration algorithms in digital image correlation. *Measurement Science and Technology*, 17(6):1615, 2006.

E. O. Brigham and R. E. Morrow. The fast fourier transform. *IEEE Spectrum*, 4(12):63–70, 1967. doi: 10.1109/MSPEC.1967.5217220.

J. Chen, K. Ji, H. Deng, and S. Feng. Analysis of correlation registration algorithms in the observation of solar magnetic field. In *Unifying Electrical Engineering and Electronics Engineering*, pages 1241–1249. Springer, 2014.

S. Das and P. N. Suganthan. Differential evolution: A survey of the state-of-the-art. *IEEE transactions on evolutionary computation*, 15(1):4–31, 2010.

M. Debella-Gilo and A. Kääb. Sub-pixel precision image matching for measuring surface displacements on mass movements using normalized cross-correlation. *Remote Sensing of Environment*, 115(1):130–142, 2011.

M. Druckmüller. Phase correlation method for the alignment of total solar eclipse images. *The Astrophysical Journal*, 706(2):1605, 2009.

M. Druckmüller, V. Rušin, and M. Minarovjech. A new numerical method of total solar eclipse photography processing. *Contrib. Astron. Obs. Skalnaté Pleso*, 36:131–148, 2006.

W. M. Elsasser. The earth's interior and geomagnetism. *Reviews of Modern Physics*, 22(1):1, 1950.

H. Foroosh, J. B. Zerubia, and M. Berthod. Extension of phase correlation to subpixel registration. *IEEE transactions on image processing*, 11(3):188–200, 2002.

P. Gilman and R. Howard. Variations in solar rotation with the sunspot cycle. *The Astrophysical Journal*, 283:385–391, 1984.

P. Gravel, J. Verhaeghe, and A. J. Reader. 3d pet image reconstruction including both motion correction and registration directly into an mr or stereotaxic spatial atlas. *Physics in Medicine & Biology*, 58(1):105, 2012.

T. Heid and A. Kääb. Evaluation of existing image matching methods for deriving glacier surface displacements globally from optical satellite imagery. *Remote Sensing of Environment*, 118:339–355, 2012.

M. Jenkinson and S. Smith. A global optimisation method for robust affine registration of brain images. *Medical image analysis*, 5(2):143–156, 2001.

M. Lefébure and L. D. Cohen. Image registration, optical flow and local rigidity. *Journal of Mathematical Imaging and Vision*, 14(2):131–147, 2001.

J. W. Leibacher, R. W. Noyes, J. Toomre, and R. K. Ulrich. Helioseismology. *Scientific American*, 253(3):48–57, 1985.

R. B. Leighton, R. W. Noyes, and G. W. Simon. Velocity fields in the solar atmosphere. i. preliminary report. *The Astrophysical Journal*, 135:474, 1962.

J. R. Lemen, D. J. Akin, P. F. Boerner, C. Chou, J. F. Drake, D. W. Duncan, C. G. Edwards, F. M. Friedlaender, G. F. Heyman, N. E. Hurlburt, et al. The atmospheric imaging assembly (aia) on the solar dynamics observatory (sdo). In *The solar dynamics observatory*, pages 17–40. Springer, 2011.

C. Leng, H. Zhang, B. Li, G. Cai, Z. Pei, and L. He. Local feature descriptor for image matching: A survey. *IEEE Access*, 7:6424–6434, 2019.

D. G. Lowe. Object recognition from local scale-invariant features. In *Proceedings of the seventh IEEE international conference on computer vision*, volume 2, pages 1150–1157. Ieee, 1999.

D. G. Lowe. Distinctive image features from scale-invariant keypoints. *International journal of computer vision*, 60(2):91–110, 2004.

M. T. Mahmood and I. H. Lee. Well-distributed feature extraction for image registration using histogram matching. *Applied Sciences*, 9(17):3487, 2019.

R. Michel and E. Rignot. Flow of glaciar moreno, argentina, from repeat-pass shuttle imaging radar images: comparison of the phase correlation method with radar interferometry. *Journal of Glaciology*, 45(149):93–100, 1999.

M. Pant, H. Zaheer, L. Garcia-Hernandez, A. Abraham, et al. Differential evolution: A review of more than two decades of research. *Engineering Applications of Artificial Intelligence*, 90:103479, 2020.

E. N. Parker. Hydromagnetic dynamo models. *The Astrophysical Journal*, 122:293, 1955.

K. V. Price. Differential evolution. In *Handbook of optimization*, pages 187–214. Springer, 2013.

E. Rublee, V. Rabaud, K. Konolige, and G. Bradski. Orb: An efficient alternative to sift or surf. In *2011 International conference on computer vision*, pages 2564–2571. Ieee, 2011.

C. Scheiner. *Rosa Ursina Sive Sol.* 1630. book 4, part 2.

C. Shapiro, B. Rowe, T. Goodsall, C. Hirata, J. Fucik, J. Rhodes, S. Seshadri, and R. Smith. Weak gravitational lensing systematics from image combination. *Publications of the Astronomical Society of the Pacific*, 125(934):1496, 2013.

M. Thompson, J. Toomre, E. Anderson, H. Antia, G. Berthomieu, D. Burtonclay, S. Chitre, J. Christensen-Dalsgaard, T. Corbard, M. DeRosa, et al. Differential rotation and dynamics of the solar interior. *Science*, 272(5266): 1300–1305, 1996.

F. Ward. *Determination of the solar-rotation rate from the motion of identifiable features*. Number 226. Air Force Cambridge Research Laboratories, Office of Aerospace Research . . . , 1966.

S. S. Young and R. G. Driggers. Superresolution image reconstruction from a sequence of aliased imagery. *Applied Optics*, 45(21):5073–5085, 2006.

R. Zappala and F. Zuccarello. Angular velocities of sunspot-groups and solar photospheric rotation. *Astronomy and Astrophysics*, 242:480–487, 1991.

X. Zhang, M. Abe, and M. Kawamata. Reduction of computational cost of poc-based methods for displacement estimation in old film sequences. *IEICE Transactions on Fundamentals of Electronics, Communications and Computer Sciences*, 94(7):1497–1504, 2011.

H. Zhou and Y. Yu. Applying rotation-invariant star descriptor to deep-sky image registration. *Frontiers of Computer Science*, 12(5):1013–1025, 2018.

ZDENĚK HRAZDÍRA

@ hrazdira.zdenek@gmail.com Brno, CZ 607 622 931 linkedin.com/in/zdenyhraz github.com/zdenyhraz

EDUCATION

PhD Student - Applied Mathematics

Faculty of Mechanical Engineering, Brno University of Technology

2018-2022

- Doctoral thesis topic: High precision sub-pixel image registration methods and their applications in astrophysics
- Development of signal/image fourier analysis based algorithms & non-continuous non-convex mathematical optimization
- Algorithm implementation in C++20 with ImGui/Qt GUI, STL, fmt, OpenCV, OpenMP, FFTW)
- University teaching - multivariable calculus, differential equations, computer graphics, statistics & mathematical software

Master's degree - Applied Mathematics

Faculty of Mechanical Engineering, Brno University of Technology

2013–2018

- Diploma thesis topic: Mutual interaction of fluid pressure pulsations and indirect pipe vibration
- Fluid-structure interaction simulation, numerical/analytical modeling with systems of coupled partial differential equations
- Modeling & calculations implemented in MATLAB

SKILL PROFILE

- C/C++, Python, MATLAB
- C++20, STL, boost, CMake, OpenCV, OpenGL, OpenMP, Qt, ImGui, CUDA, FFTW, fmt, blaze, NumPy, PyTorch, LibTorch, Matplotlib, gtest, gbenchmark
- Linux, Windows, GDB, Visual Studio Code, Visual Studio, Git, CI/CD, GitHub, GitLab, Azure, Jira, conan, vcpkg, LaTeX
- Software design patterns, multithreading, performance benchmarking/profiling, optimization, code quality, maintainability, flexibility
- Mathematical modeling, numerical methods, statistical methods, Fourier analysis, differential & algebraic equations, continuous & non-continuous convex & non-convex global optimization, signal processing
- Machine learning - evolutionary algorithms, ANNs, CNNs, computer vision
- Image processing - filtering, 2D Fourier analysis, sub-pixel image registration, feature detection
- UI/UX - Qt/QCustomPlot, ImGui/ImPlot
- Languages - English (fluent), German (limited), Czech (native)

EXPERIENCE

Senior Software Scientist

Thermo Fisher Scientific

2021-2022 Brno, CZ

- Mass spectrometry instrument control software architecture design & development
- C++20, Python, Linux

C++ Software Developer & Researcher

Phonexia

2020-2021 Brno, CZ

- Development of high performance voice biometrics and speech recognition machine learning solutions
- Speech recognition research, modern software design and implementation with emphasis on performance, modularity and testability
- C++17/20, Linux

Advanced Technology Scientist Intern

Thermo Fisher Scientific

2017-2019 Brno, CZ

- Charged particle optics, numerical particle tracing, applications of mathematical non-convex optimization methods for electron beam alignment
- C++14, Windows

LICENSES & CERTIFICATIONS

Convolutional Neural Networks and Image Processing

Machine Learning College

Computer Vision with Embedded Machine Learning

Coursera